

Dynamics of a millimeter size drop exposed to MHz-frequency surface acoustic wave in the underlying solid substrate

Y. Li¹, J.A. Diez², J. D'Addesa³, O. Manor¹, L.J. Cummings³, L. Kondic³

¹ Department of Chemical Engineering, Technion - Israel Institute of Technology, Haifa 32000, Israel

² Instituto de Física Arroyo Seco, Universidad Nacional del Centro de la Provincia de Buenos Aires, 7000 Tandil, Argentina

³ Department of Mathematical Sciences and Center for Applied Mathematics and Statistics, New Jersey Institute of Technology, Newark, New Jersey 07102, USA

We present an experimental, theoretical, and computational study of the spreading of a millimetric silicon oil drop under the excitation of a surface acoustic wave (SAW), traveling in the underlying solid substrate. Our fully time-dependent theoretical model is formulated within the long wave approach, and accounts carefully for the interaction between fluid dynamics and acoustic driving. While an approach similar to ours was used in previous works to analyze the dynamics of micron-scale films of oil and water under SAW excitation, the acoustic forcing was associated with boundary layer flow, i.e., Schlichting and Rayleigh streaming, and with acoustic radiation pressure. For the case considered here (millimetric thickness drops), the acoustic forcing is related to the Eckart streaming; the forcing mechanism is a result of variations in the Reynolds stress in the liquid, which is associated with variations in the intensity of ultrasonic wave leakage off the attenuating SAW under the drop. Schlichting and Rayleigh streaming contributions are usually negligible in this case. We find, in both experiments and simulations, that following an initial transient, where the oil drop deforms to accommodate the acoustic stress therein, the drop accelerates to reach translation at approximately constant speed for long times, while leaving a thin wetting layer behind. Our model suggests that the drop's steady speed is due to the quasi-steady shape of the drop's main body at long times, which is itself a consequence of the rate of SAW attenuation, which depends on the thickness of the liquid body above. The SAW attenuation is weak under air and the micron-thick liquid trail left behind the drop; it becomes significant once the SAW reaches the main body of the drop. Hence, the forcing on the drop is approximately the same, irrespective of its distance to the source of the SAW. The translating drop's speed is found to be dependent on the drop size, as well as on the SAW intensity. The drop's steady shape and speed are further informed by analytical consideration of a simplified traveling wave type model, that clarifies contributions from different physical effects. The theoretical results show qualitative and sometimes even quantitative agreement with the experiments, particularly regarding drop height and traveling speed.

I. INTRODUCTION

Dynamic wetting of a solid substrate by a liquid film is a common occurrence. In natural systems, it appears in surfactant films that wet the lungs to promote breathing and the eyes to keep them moist [1, 2], or in the spreading of water drops on solid surfaces (such as raindrops on windows) [3, 4]. In technological systems it is harnessed for actuating microfluidic platforms [5, 6, 7], for cooling electronic circuits [8, 9], for desalination [10] and for a variety of manufacturing applications [11, 12, 13]. Many different mechanisms govern dynamic wetting, where capillary forces at the free surface of a liquid film or a meniscus contribute appreciably to the dynamics of the film. In addition to capillary forces, dynamic wetting may be powered by gravity, thermal or solutal Marangoni effects, or electrokinetics, among others, see Oron *et al.* [14] or Craster and Matar [15] for comprehensive reviews. In the present work, we focus on the contributions of mechanical vibrations in the solid substrate, particularly MHz-frequency Rayleigh surface acoustic waves (SAWs), to dynamic wetting [16]. We study particularly the effects of Eckart streaming – mass transport in the bulk fluid that results from variations in acoustic or ultrasonic intensity. While extensively observed and described in the scientific literature [17, 18, 19], we are not aware of a model describing the dynamics of such a system that further accounts for the capillary and gravitational stresses that shape the liquid/air interface for the case when drops are sufficiently thick (millimeter scale). Here, we use thin film (long wave) theory alongside physical experiments to develop a better understanding of the dynamics of this problem.

There are several different mechanisms by which acoustic waves or other mechanical waves, at a solid boundary or at the free surface of a liquid, generate streaming – steady flow along the wave's path. A mechanical wave at a boundary invokes periodic viscous flow within the viscous penetration length $\delta \equiv \sqrt{2\mu/(\rho\omega)}$ away from the interface, where μ , ρ and ω are the viscosity and density of the liquid, and the wave angular frequency, respectively. Examples in which this problem was considered include the work by Rayleigh on a standing acoustic wave grazing a solid bed [20]; by Schlichting [21] on standing vibration of waves of infinite and finite (respectively) wavelength in a solid along its surface; by Longuet-Higgins [22] on shallow ocean waves; and by Manor *et al.* [23] on propagating Rayleigh (surface acoustic) waves in a solid substrate. Convective contributions due to surface waves invoke a drift of liquid mass, which

does not attenuate away from the solid surface. It is known as Schlichting streaming [19], and its component far from the boundary was further coined the ‘‘Rayleigh law of streaming’’ by Lighthill [24] in recognition of Rayleigh’s work on the drift resulting from the presence of standing acoustic waves in fluid near a solid boundary.

Another mechanism, the Eckart streaming – the focus of the current work – appears regardless of the presence of a boundary. Eckart streaming results from *variations* of the intensity of sound or ultrasound waves in the fluid. In the classic work by Eckart and in many subsequent studies, the Eckart streaming is ascribed to the viscous attenuation of traveling sound waves in the fluid [24, 25, 26]. This attenuation results in spatial variations of the fluid velocity field, and therefore in the convective Reynolds stresses. The consequence is the occurrence of a secondary flow whose steady component at long times is the acoustic streaming. Eckart streaming is characterized by an intense vortical flow field that appears in the bulk fluid. This is the main acoustic mechanism for the actuation of fluid in micro-channels [19, 27, 28] and in drop microfluidics [17, 18, 29, 30]. It usually dominates contributions to the flow in the bulk fluid arising from the boundary layer type acoustic streaming mechanisms (such as Schlichting or Rayleigh streaming described above).

Approximately 40 years after Eckart’s work, Shiokawa *et al.* [31] considered MHz-frequency SAWs that travel in a solid and leak same-frequency ultrasonic waves into the fluid. In this scenario, they showed that the main contribution to spatial variations in wave intensity in the fluid and, hence, to variations in the Reynolds stress arises from the fast attenuation of surface acoustic waves (SAWs) in the neighboring solid substrate. Moreover, the SAW attenuation is faster than that of the viscous attenuation of the ultrasound leakage waves as they travel in the fluid. Thus, to leading order, variation in the intensity of ultrasound leakage in the fluid results from SAW attenuation in the solid. For example, 20 MHz frequency SAWs traveling in a solid substrate in contact with a thick layer of water at ambient conditions possess an attenuation length of approximately 2 millimeters [32]. However, the same frequency ultrasonic waves in bulk water possess an attenuation length of approximately 100 millimeters [33]. Hence, in contrast to the assumptions in Eckart’s original work on acoustic streaming, the Reynolds stress variation in a fluid in contact with a leaky SAW is to leading order correlated with the attenuation of the SAW in the solid, rather than with the viscous attenuation of the ultrasound wave leakage in the fluid.

In addition to the flow mechanisms discussed above, the presence of an acoustic wave in a liquid, whether due to an actuator or an acoustic wave in the solid, leads to acoustic radiation pressure [31, 34, 35, 36, 37]. Convective effects (Reynolds stresses) within the wave increase the local steady pressure in the bulk of the liquid; upon reflection of the wave at an interface between phases of mismatched acoustic impedance (density multiplied by acoustic phase velocity), the wave imposes convective stress – acoustic radiation pressure [38, 39, 40] – capable of deforming and displacing the interface [41, 42, 43]. There are abundant studies on the dynamic wetting of thin liquid films that are governed by Schlichting and Rayleigh streaming, alongside acoustic radiation pressure. For example, SAWs were recently shown to power the continuous spreading of sub-micrometer to tens of micrometers thick films of fully wetting silicon oils [44, 45] and partially wetting water/surfactant mixtures [46, 47, 48] along or opposite the path of the propagating SAW. However, we are unaware of studies that consider the acoustic/capillary balance of dynamic wetting in liquid films and drops that are sufficiently thick that mass transport therein, and hence film dynamics, are actuated by Eckart streaming. Consideration of such a regime is the subject of the present paper.

In this paper, we use theory and simulations, which we compare to our physical experiments, to elucidate the physics of dynamic wetting powered by Eckart streaming under the action of MHz-frequency Rayleigh-type SAWs. We describe our experiments in Sec. II and then derive the theoretical model in Sec. III. Our theoretical results are presented in Sec. IV: we discuss computational results in Secs. IV A and IV B, before analyzing a simplified traveling-wave type model in Sec. IV C. Section V is devoted to the summary and conclusions.

II. EXPERIMENT

Figure 1 shows the experimental setup. We generate a propagating 20 MHz frequency surface acoustic wave (SAW) by applying a same-frequency sinusoidal voltage signal to a piezoelectric actuator – a SAW device. The actuator comprises a 5 nm titanium/1 μm aluminum interdigitated transducer (IDT; from which the SAW emanates) fabricated atop lithium niobate (LiNbO_3 , Roditi International, UK) by standard lift-off photolithography. The substrate used for the SAW device is 11 mm \times 24 mm in size, 0.5 mm thick, 128° Y-cut, X-propagating, single-crystal piezoelectric lithium niobate, where X and Y are crystal axes [49]. The actuator is integrated into the external electrical signal using pogo pins (BC201403AD, Interconnect Devices, Inc.) assembled in a 3D-printed elastomeric stage, which holds the actuator and is connected to a signal generator (R&S SMB100A microwave signal generator) and amplifier (model A10160, Tabor Electronics Ltd.). We place a paper cylinder soaked with glycerol at the far end of the actuator from the IDT. The glycerol-soaked paper absorbs the SAW and prevents reflections. We measure the SAW normal surface vibration at the actuator surface and verify that it is a propagating wave using a scanning laser Doppler vibrometer (MSA-500, Polytech).

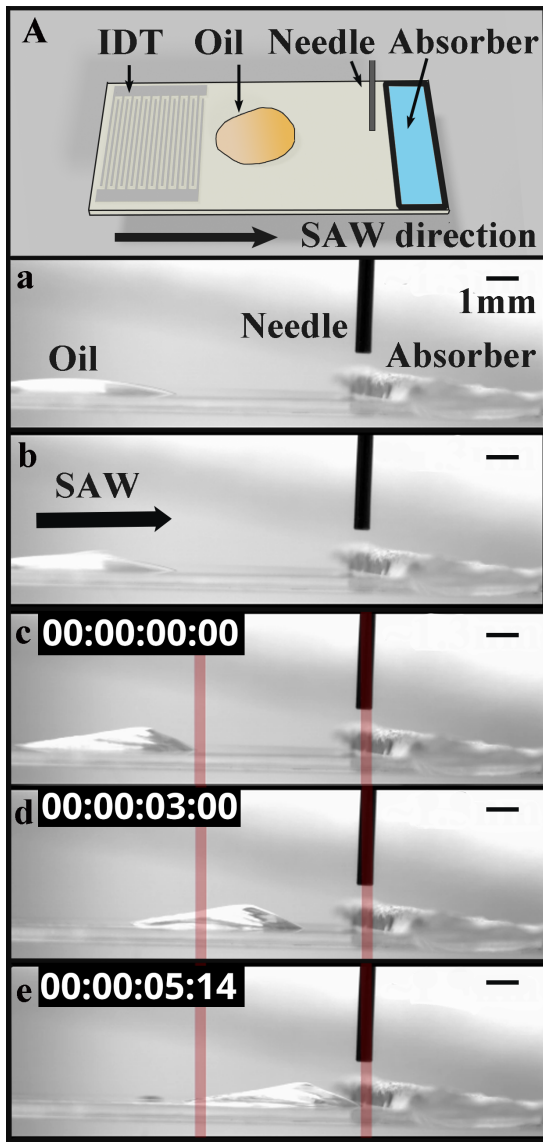


FIG. 1. (A) Upper schematic view of the experimental setup: Surface acoustic wave (SAW) propagates from the interdigitated transducer (IDT) until it reaches the acoustic absorber (comprised of glycerol-soaked paper placed on the actuator under and to the right of the needle). The needle is of known diameter ($510 \mu\text{m}$), placed for identifying spatial resolution in the images. (a-e) Successive snapshots are taken from an experiment monitoring the flow of a silicone oil film. During the experiment, a drop of silicone oil is placed on the horizontal surface (a), it deforms due to the application of SAW (b), and moves in the direction of SAW propagation (c-e); time is shown in seconds, and the vertical lines serve as a reference.

We place an 8 mm^3 ($8 \mu\text{l}$) puddle of silicone oil (50 cSt, 378356, Sigma-Aldrich) atop the actuator using a pipette, approximately 3.5 mm away from the IDT, and introduce electrical signal at different voltage levels to induce motion of the oil film, which dynamically wets the solid substrate along the path of the SAW. Figure 2(a-c) shows a time-lapse (side view) of the silicone oil dynamics, captured using the framework and camera of a goniometer (Data Physics; OCA 15Pro). Figure 2(d) shows a top view obtained using a camera (EOS R5, Canon) with a macro lens (RF 100 mm F2.8L MACRO IS USM, Canon). Prior to the experiment we clean the SAW device using four different solvents: acetone (AR-b, 99.8%, 67-641, Bio-Lab Ltd.), 2-propanol (AR-b, 99.8%, 67-63-0, Bio-Lab Ltd.), ethanol (CP-p, 96%, 64-17-5, Bio-Lab Ltd.), and water (HPLC plus, 7732-18-5, Sigma-Aldrich). Finally, we dry the actuator using compressed air.

In our experiments, we vary the SAW displacement amplitude A (normal amplitude at the solid surface before any attenuation) at the surface of the actuator by varying the applied voltage level input to the SAW device (there is a linear relationship between the two; see Appendix A for the corresponding calibration graph). To confirm that the

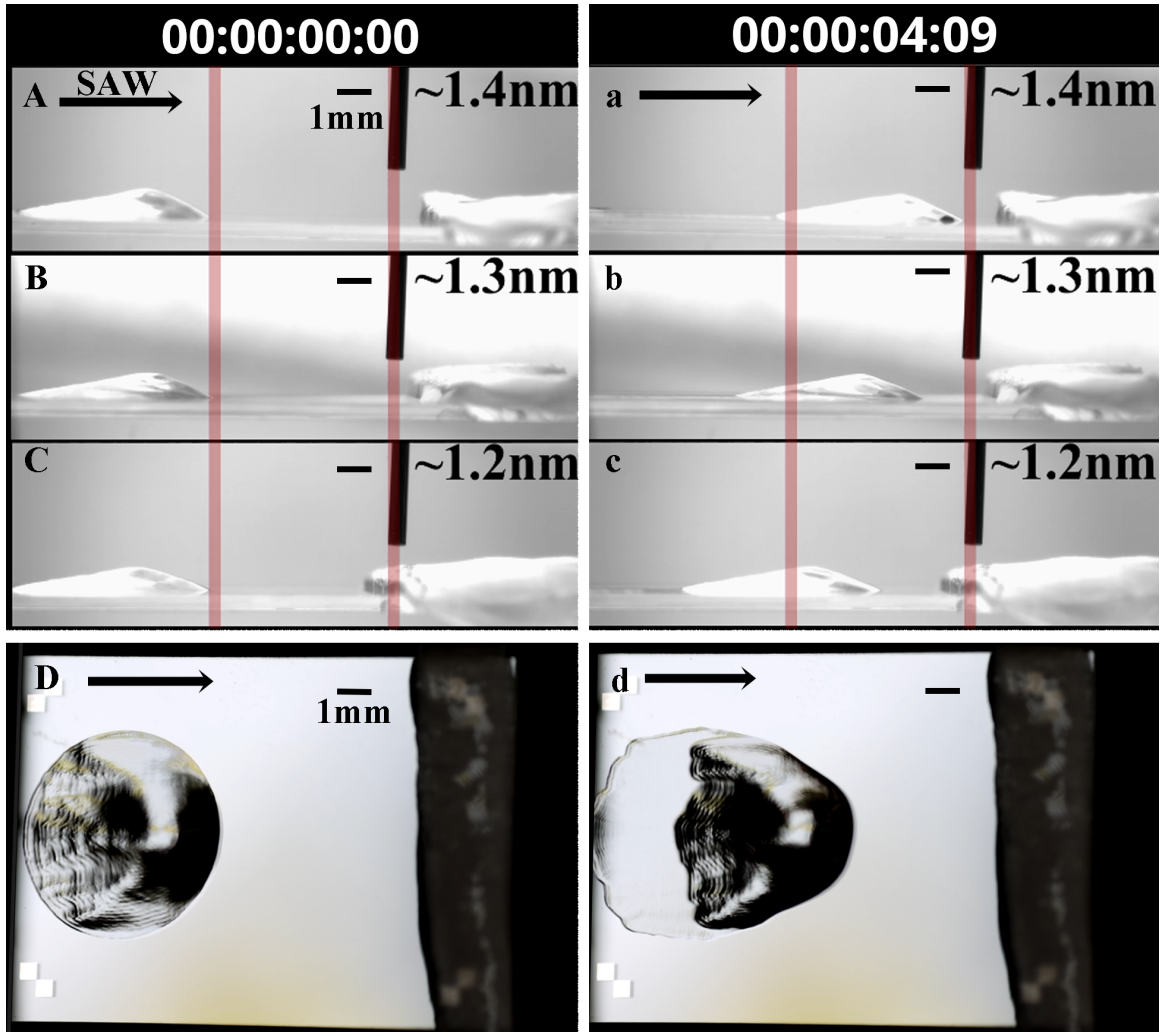


FIG. 2. Two sets of images from experiments monitoring silicone oil powered by SAWs of three different amplitudes A (1.2 nm–1.4 nm), where (A-C) silicone oil starts from the same location, moves in the direction of the SAW, and reaches different distances (a-c) after 4.09 seconds. The corresponding side-view videos at different acoustic power levels are used to analyze the speed and profile of silicone oil during the movement. (D, d) show top view snapshots (corresponding to (C,c)) of the oil. A thin film of oil, hardly visible in the side view, can be seen more clearly behind the main body of silicone oil in the top views.

observed dynamics are indeed induced by SAW, we also carried out control experiments, shown in Fig. 3, in which SAW is absent and all other parameters are kept the same. The oil puddle in this experiment, which was repeated three times, slowly spreads concentrically, as expected in the absence of a directional forcing mechanism.

We employ the side view video, recorded by a goniometer camera, to capture the position of the advancing three-phase contact line of the SAW-actuated oil film using the open-source software *Tracker* [50] (see Fig. 4(a) for typical data). We also measure the maximum height of the moving oil film using the public domain image processing software *ImageJ* (typical results in Fig. 4(b)). Figure 4(a) shows that, as expected, the larger the SAW amplitude A , the faster the oil film moves due to the stronger induced leakage wave [31]. Another notable aspect of SAW-induced dynamics is the contact line speed for early times (< 1 s): initially, it is rather small, but later increases and then remains constant. This change of contact line speed appears to be a consequence of the initial change of shape of the drop (see also Fig. 1); while this is taking place, contact line speed is small. After the initial deformation, the drop shape remains unchanged, translating approximately uniformly (this will be seen in Fig. 9 later in the text). Figure 4(b) shows consistent results for the maximum drop height, with an increase of the height for early times, and constant values for longer times. Note that this uniform translation and constant film height differ significantly from the observed behavior for spreading under a body force such as gravity (for gravity-driven spreading such as in Fig. 3 the contact line speed decreases, and the drop becomes thinner as it spreads). These experimental observations will be explained and discussed within the framework of our theoretical model, which is described next.

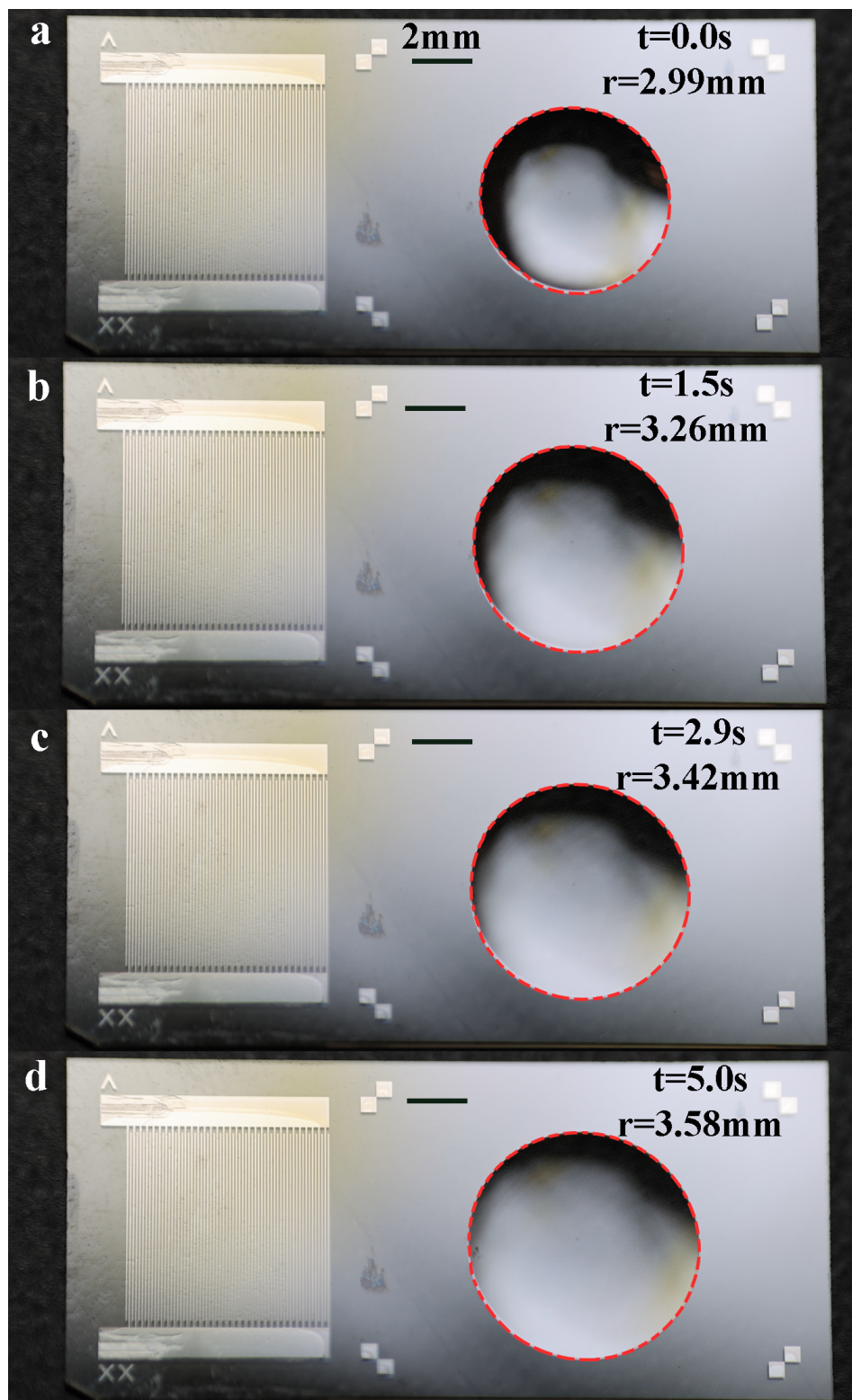


FIG. 3. Successive snapshots taken from the baseline experiments monitoring silicone oil spreading without a SAW, where the outline of the oil drop is marked as a red dashed line. The time/radius stamps are given at the top right corner of each figure part.

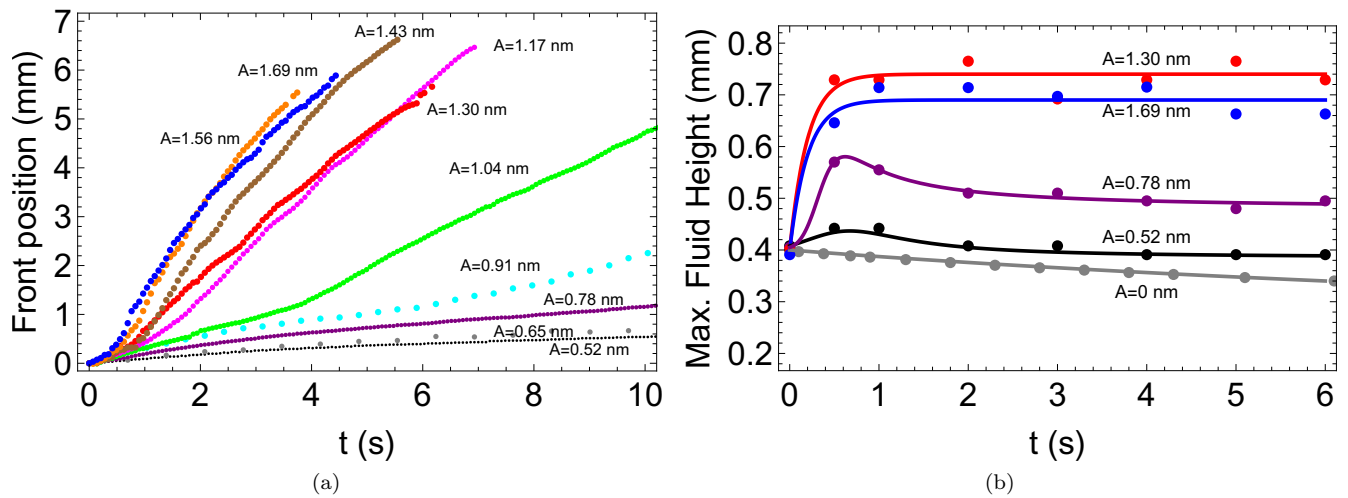


FIG. 4. (a) Time evolution of the front position for several values of $A = 0.52$ nm (black), 0.65 nm (gray), 0.78 nm (purple), 0.91 nm (cyan), 1.04 nm (green), 1.17 nm (magenta), 1.30 nm (red), 1.43 nm (brown), 1.56 nm (orange), 1.69 nm (blue). (b) Time variations of the maximum drop height for $A = 0$ nm (gray, no SAW applied), 0.52 nm (black), 0.78 nm (purple), 1.30 nm (red) and 1.69 nm (blue). The symbols correspond to the measurements and the lines are simple fits to guide the eye. We expect errors of ± 50 μm in the values of the film height due to the limited resolution of the side view image and tracker software.

III. MODEL

To model the experiments described in Sec. II, we consider a fluid traversed by a sound wave. The fluid velocity, \mathbf{V} , can be written as

$$\mathbf{V} = \mathbf{v} + \mathbf{v}_s, \quad (1)$$

where \mathbf{v} is the “bulk” velocity of the fluid, associated with a characteristic time of the flow, t_c , which is on the order of seconds (so $|\mathbf{v}| \sim \ell/t_c$, if ℓ is a typical lengthscale of the flow); and \mathbf{v}_s is associated with the much faster timescale of the sound wave, $T = f^{-1} \ll t_c$ (typically $T \sim 10^{-6}$ s). The idea behind Eq. (1) is that \mathbf{v}_s corresponds to an oscillatory flow generated by the propagating sound wave, while \mathbf{v} is the velocity due to external forces (or to the wave propagation itself, as we will show below). Therefore, the fast-time averages, $\langle \cdot \rangle = (1/T) \int_0^T \cdot dt$, of \mathbf{v} and \mathbf{v}_s , are given by

$$\langle \mathbf{v} \rangle \approx \mathbf{v}, \quad \langle \mathbf{v}_s \rangle = 0. \quad (2)$$

We write the Navier–Stokes (NS) equations for the fluid in the compact form

$$\frac{\partial(\rho\mathbf{V})}{\partial t} + \rho(\mathbf{V} \cdot \nabla)\mathbf{V} + \mathbf{V}\nabla \cdot (\rho\mathbf{V}) = -\nabla p + \mu\nabla^2\mathbf{V} + \left(\zeta + \frac{\mu}{3}\right)\nabla(\nabla \cdot \mathbf{V}), \quad (3)$$

where ρ is the density of a compressible fluid and μ , ζ are the first and second dynamic viscosities, respectively. Since we seek the resulting flow field for large times (of the order of t_c), we take the fast-time average of Eq. (3) as defined above. Thus, using Eqs. (1) and (2), we find

$$\frac{\partial(\rho\mathbf{v})}{\partial t} = -\nabla p + \mathbf{F}_s + \mu\nabla^2\mathbf{v} + \left(\zeta + \frac{\mu}{3}\right)\nabla(\nabla \cdot \mathbf{v}), \quad (4)$$

where

$$\mathbf{F}_s = -\langle \rho_0(\mathbf{v}_s \cdot \nabla)\mathbf{v}_s + \mathbf{v}_s\nabla \cdot (\rho_0\mathbf{v}_s) \rangle, \quad (5)$$

and $\rho_0 = \langle \rho \rangle$ is the average (constant) density of the fluid (note that $\langle \partial(\rho_0\mathbf{v}_s)/\partial t \rangle = 0$). Equation (4) shows that the flow field \mathbf{v} , which develops on the long time scale t_c , satisfies NS equations similar to those for \mathbf{V} , but with an additional volume force, \mathbf{F}_s . This flow field, \mathbf{v} , is known as *acoustic streaming flow*, resulting from the high-frequency

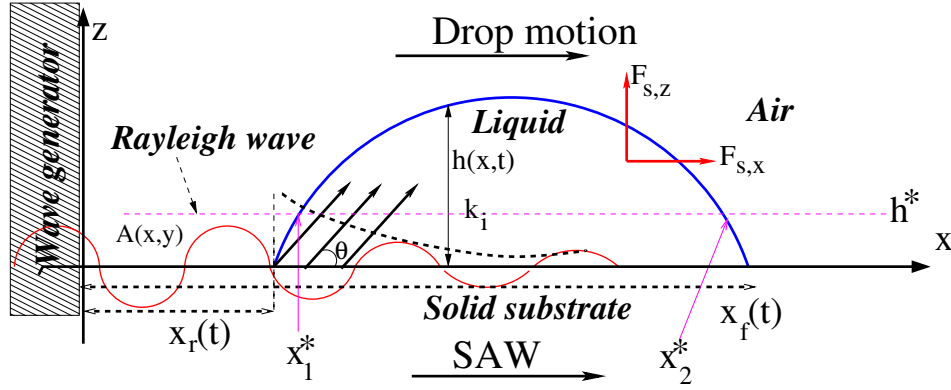


FIG. 5. Schematic of a liquid drop (blue curve) forced by a SAW traveling from left to right, with *rear* and *front* contact lines at $x_r(t)$ and $x_f(t)$, respectively. The thin red line represents the amplitude A of the leaky SAW at the substrate and shows how it is attenuated by liquid (the black dashed line is the envelope of the decaying amplitude in the liquid). The Rayleigh angle is denoted by θ .

sound wave traversing the fluid (see, e.g. [31]). As we pointed out in the Introduction, this acoustic streaming flow corresponds to the Eckart streaming due to the Reynolds stress variation in the fluid caused by SAW attenuation in the solid.

When the sound wave is a leaky wave generated at a solid substrate that propagates in the (x, z) -plane (see Fig. 5), the fluid particle displacement, \mathbf{u} , can be written as [51] (we discuss later in this section the assumptions behind this formulation)

$$u_x = \Re \left[A e^{\iota(k_L x' - \omega t) + \iota \alpha_1 k_L z} \right] = A e^{-k_i x' - \alpha_1 k_i z} \cos [k_r x' + \alpha_1 k_r z - \omega t], \quad (6)$$

$$u_y = 0, \quad (7)$$

$$u_z = \alpha_1 u_x, \quad (8)$$

where A is the wave amplitude, $k_L = k_r + \iota k_i$ is the complex wavenumber of the leaky wave and $x' = x - x_{\text{ref}}(t)$, where $x_{\text{ref}}(t)$ is a reference x -coordinate determining the onset of attenuation, whose origin will be discussed in Sec. IV. Also, we define

$$\alpha_1 = \sqrt{(c_s/c_{\text{oil}})^2 - 1}, \quad (9)$$

where c_s and c_{oil} are the SAW phase velocities in the substrate and silicon oil, respectively. By choosing [52] $c_s = 3880$ m/s and [53] $c_{\text{oil}} = 1350$ m/s, we obtain $\alpha_1 = 2.69$. Thus, the Rayleigh angle θ is given by $\theta = \arctan \alpha_1 = 69.65^\circ$. The SAW attenuation factor is given by [32]

$$k_i = \frac{1}{l_i} = \frac{\rho_{\text{oil}}}{\rho_s} \frac{c_{\text{oil}}}{c_s^2} f, \quad (10)$$

where l_i is the attenuation length (of the SAW in the solid), and ρ_s is the solid density. For the experimental values: $f = 20$ MHz, $\rho_s = 4.65$ g/cm³ and $\rho_{\text{oil}} = 0.96$ g/cm³, we obtain $l_i = 2.7$ mm. Note that the SAW wavelengths in the solid substrate and the oil are $\lambda_s = c_s/f = 194$ μm and $\lambda_{\text{oil}} = c_{\text{oil}}/f = 67.5$ μm , respectively.

The fluid particle displacement in Eqs. (6)–(8) is related to the Eulerian velocity field, $\mathbf{v}_s = (v_{s,x}, v_{s,y}, v_{s,z})$, by

$$v_{s,x} = \frac{du_x}{dt}, \quad v_{s,y} = \frac{du_y}{dt}, \quad v_{s,z} = \frac{du_z}{dt}, \quad (11)$$

which, on substitution into Eq. (5), leads to explicit expressions for the force components (note that we use $\rho_0 = \rho_{\text{oil}}$ from now on to avoid confusion),

$$F_{s,x} = (1 + \alpha_1^2) k_i \rho_{\text{oil}} A^2 \omega^2 e^{-2k_i(x' + \alpha_1 z)}, \quad (12)$$

$$F_{s,y} = 0, \quad (13)$$

$$F_{s,z} = \alpha_1 F_{s,x}. \quad (14)$$

The force \mathbf{F}_s is conservative, i.e., it can be expressed as $\mathbf{F}_s = -\nabla\phi_s$ where the potential, ϕ_s , is given by

$$\phi_s(x, z) = \phi_0 e^{-2k_i(x' + \alpha_1 z)}, \quad \text{with} \quad \phi_0 = \frac{1 + \alpha_1^2}{2} \rho_{\text{oil}} A^2 \omega^2. \quad (15)$$

Therefore, the NS equations (4) for the velocity field \mathbf{v} , under the influence of both SAW and gravitational forces, can be written as

$$\rho_{\text{oil}} \frac{\partial \mathbf{v}}{\partial t} = -\nabla P + \mu \nabla^2 \mathbf{v}, \quad (16)$$

where we assume that the \mathbf{v} field is incompressible ($\nabla \cdot \mathbf{v} = 0$), and we have defined the *effective pressure*, P , as

$$P = p + \phi_s + \phi_g, \quad (17)$$

with ϕ_s given by Eq. (15) and $\phi_g(z) = \rho_{\text{oil}} g z$, corresponding to a gravitational body force, $\mathbf{F}_g = -\nabla\phi_g = -\rho_{\text{oil}} g \hat{\mathbf{k}}$, where $\hat{\mathbf{k}}$ is a unit vector in the out-of-plane direction.

We now briefly discuss the assumptions of the model presented so far. Our focus is on modeling drops of millimetric thickness, as considered in our experiments. Therefore, we focus on the Eckart streaming that dominates at these length scales; that is, the variation of the acoustic field in the solid caused by attenuation of SAW in the solid substrate, as discussed in the Introduction and as considered thus far in our presentation. We recall that, very close to the solid surface, there is a boundary layer flow governed by Schlichting and Rayleigh streaming, in which Eckart streaming is negligible. These Schlichting and Rayleigh mechanisms are observed to support spreading on lengthscales $\lambda_{\text{oil}}/4$ or less [44, 45, 46, 47], which is much smaller than the drop thickness relevant to our experiments. These effects are therefore not included in our formulation, except that in our implementation (described in Sec. IV), we assume that the SAW experiences no attenuation in regions where the film thickness is smaller than this value so that Eckart streaming does not act in such regions.

We also ignore contributions from acoustic radiation pressure. To justify this approximation, we note that the stress associated with acoustic radiation pressure due to a traveling acoustic wave is characterized by [35] $(1/2 + B/(4C)) \rho_{\text{oil}} (\omega A)^2$, where B and C are the Fox and Wallace coefficients for the non-linear adiabatic connection between pressure and fluid density. For our experiments, $(1/2 + B/(4C)) \approx 3$, given that $B/C \approx 10$ for organic liquids at room temperature [54]. On the other hand, the characteristic stress associated with Eckart-type acoustic streaming is approximately $(l_i f/c_s) \rho_{\text{oil}} (\omega A)^2$, noting again that l_i and f/c_s are the attenuation length and the wavelength of the SAW. The product $l_i f/c_s = (\rho_s/\rho_{\text{oil}}) (c_s/c_{\text{oil}}) \approx 16$, using the experimental values of the parameters given after Eq. (10). Hence, as long as the liquid drop is sufficiently thick to support Eckart streaming (as is the case in our experiments, where the drops are of millimetric thickness), and while its surface is curved so that acoustic resonance effects that may result in high acoustic radiation pressure levels are avoided, the stresses that contribute to flow due to the Eckart streaming mechanism are an order of magnitude larger than contributions from acoustic radiation pressure.

In this work, we consider incompressible, low Reynolds number free surface flows under the long-wave approximation so that all inertial terms on the left-hand side of Eqs. (16) are negligible with respect to the viscous and pressure terms. Carrying out a standard long-wave expansion of Eqs. (16) and imposing the usual stress boundary conditions at the free surface (vanishing tangential stress and normal stress balanced by surface tension, see e.g. [55] for details), we obtain the following fourth-order differential equation for the film height, $z = h(x, y, t)$,

$$3\mu \frac{\partial h}{\partial t} - \nabla \cdot (h^3 \nabla P) = 0, \quad (18)$$

where

$$P(x, y, t) = -\gamma \nabla^2 h + \rho_{\text{oil}} g h + \phi_s(x, h). \quad (19)$$

Here, γ is the coefficient of surface tension at the oil-air interface, assumed constant.

We nondimensionalize the problem using an arbitrary length scale, ℓ , a timescale t_c such that leading order terms balance in Eq. (18), and a pressure scale p_c based on the capillary contribution in Eq. (19), so that we have

$$(x, y) = \ell(\tilde{x}, \tilde{y}), \quad (x_{\text{ref}}, h) = \ell(\tilde{x}_{\text{ref}}, \tilde{h}), \quad t = t_c \tilde{t} = \frac{3\mu\ell}{\gamma} \tilde{t}, \quad P = p_c \tilde{P} = \frac{\gamma}{\ell} \tilde{P}, \quad (20)$$

where the tilded quantities are dimensionless. Thus, the dimensionless governing equation is

$$\frac{\partial \tilde{h}}{\partial \tilde{t}} - \tilde{\nabla} \cdot (\tilde{h}^3 \tilde{\nabla} \tilde{P}) = 0, \quad (21)$$

where

$$\tilde{P} = -\tilde{\nabla}^2 \tilde{h} + \text{Bo} \tilde{h} + \mathcal{S} \tilde{\phi}_s(\tilde{x}, \tilde{h}), \quad (22)$$

with

$$\tilde{\phi}_s(\tilde{x}, \tilde{h}) = e^{-2\tilde{k}_i[(\tilde{x}-\tilde{x}_{\text{ref}})+\alpha_1 \tilde{h}]}, \quad (23)$$

and we have defined $\tilde{k}_i = \ell k_i$. The dimensionless parameters introduced here are given by

$$\text{Bo} = \frac{\rho_{\text{oil}} \ell^2}{\gamma} g = \frac{\ell^2}{a^2}, \quad \mathcal{S} = \frac{\ell}{\gamma} \phi_0, \quad (24)$$

where $a = \sqrt{\gamma/(\rho_{\text{oil}}g)}$ is the capillary length and ϕ_0 was defined in Eq. (15). In our simulations, motivated by a typical drop size in the experiments, we set $\ell = 1$ mm. For simplicity, we omit the tilde from now; all variables are dimensionless unless specific units are explicitly given, mainly when comparison with experimental data is required.

IV. THEORETICAL RESULTS

In this section, we discuss the predictions of the model developed in Sec. III, and compare them with the experimental results. In Sec. IV A, we present results for a chosen reference case, and then in Sec. IV B, we discuss the influence of model parameters, in particular the acoustic amplitude, on the results. In Sec. IV C we discuss (approximate) traveling-wave solutions. All simulations are carried out in two physical dimensions, assuming translational invariance in the transverse y -direction. The discussion of three-dimensional effects will be presented elsewhere.

A. Main features of the results

In our simulations, we solve Eq. (21) numerically using COMSOL™; see Appendix B for the description of the implementation. As the initial condition, we consider the two-dimensional parabolic drop of cross-sectional area

$$A_d = 2 \int_0^{r_d} h_d \left[1 - \left(\frac{x}{r_d} \right)^2 \right] dx = \frac{4}{3} h_d r_d, \quad (25)$$

which remains constant during the drop evolution. The drop height parameter h_d is obtained from the known experimental (3D) drop volume, V_d , as $h_d = 2V_d/(\pi r_d^2)$, using the formula for the volume V_d of a 3D parabolic cap of base radius r_d and height h_d . The 2D parabolic initial condition is centered at $x = x_d$, and is written as

$$h(x, 0) = \begin{cases} h_p, & x < x_r(0), \\ (h_d - h_p) \left[1 - \left(\frac{x-x_d}{r_d} \right)^2 \right] + h_p, & x_r(0) \leq x \leq x_f(0), \\ h_p, & x > x_f(0), \end{cases} \quad (26)$$

where $x_r(0) = x_d - r_d$ and $x_f(0) = x_d + r_d$ are the initial positions of the rear and front contact lines of the drop, respectively (see Fig. 5). Here, h_p ($\ll h_d$) is the thickness of a precursor film, introduced for numerical reasons in order to avoid the stress singularity associated with a moving contact line. It is well known (see, e.g. [56]), that the step size Δx in the spatial discretization should be similar to h_p to ensure numerical convergence, and therefore we use $\Delta x = h_p$ in our simulations. The specific value assigned to h_p has only a minor influence on the results; e.g., if h_p is doubled or halved, the change of spreading speed or drop height is just 1-2%. All reported results are obtained using $h_p = 0.01$.

Recalling the introduction of the reference x -coordinate origin, $x_{\text{ref}}(t)$, in Sec. III, we note that the SAW experiences minimal attenuation in regions of the actuator where fluid is not present, with significant attenuation only under the bulk droplet. To model this, we assume that the acoustic potential, ϕ_s , is constant (no attenuation) in regions where the film height is smaller than some critical thickness h^* , and attenuates where $h > h^*$,

$$\phi_s = \begin{cases} 1, & x < x_1^*(t), \\ e^{-2k_i[x-x_1^*(t)+\alpha_1(h-h^*)]}, & x_1^*(t) \leq x \leq x_2^*(t), \\ e^{-2k_i[x_2^*(t)-x_1^*(t)]}, & x > x_2^*(t), \end{cases} \quad (27)$$

Experiment	Simulation
$\rho_{\text{oil}} = 0.96 \text{ g/cm}^3$	$\mathcal{S} = 5.087$
$\mu = 0.5 \text{ Poise}$	$\text{Bo} = 0.452$
$\gamma = 20.8 \text{ dyn/cm}$	$A_d = 2.12$
$\omega = 2\pi \times 20 \text{ MHz}$	$r_d = 3.2$
$A = 1.3 \text{ nm}$	$h_d = 0.497$
$l_i = 2.7 \text{ mm}$	$k_i = 0.37$
$\ell = 1 \text{ mm}$	$h_p = 0.010$
	$h_* = 0.017$

TABLE I. Dimensional parameters of the experiments and the corresponding dimensionless constants used in the simulations for an 8 mm^3 volume drop.

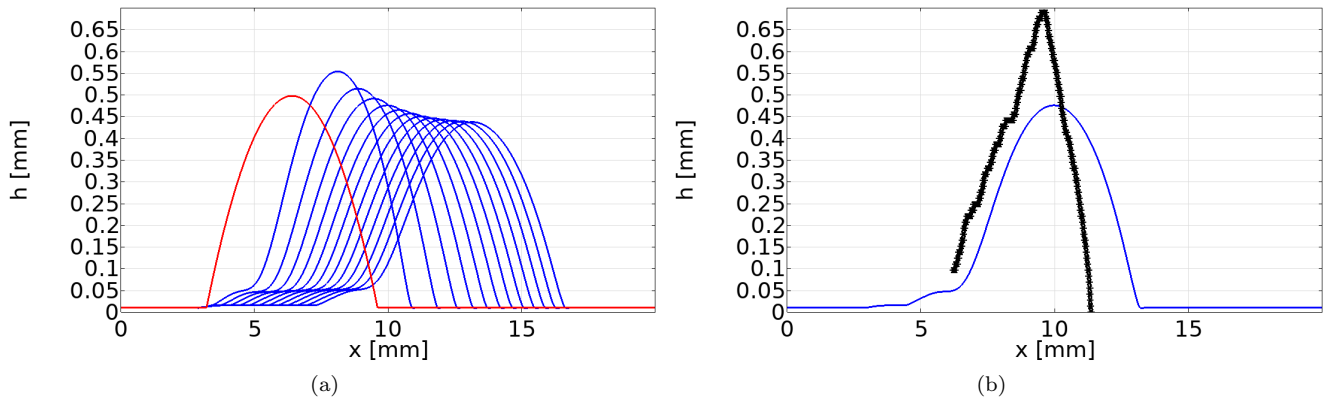


FIG. 6. (a) Thickness profiles from $t = 0$ (red line) to $t = 6$ s every $\Delta t = 0.5$ s for $A = 1.30$ nm. Here, we use $h^* = 17 \mu\text{m}/\ell \approx (\lambda_{\text{oil}}/4)/\ell$. (b) Comparison between simulated (solid blue line) and experimental (black symbols) thickness profiles at $t = 2$ s.

where x_1^* , x_2^* are defined by $h(x_1^*, t) = h(x_2^*, t) = h^*$ (this form of ϕ_s corresponds to the choice $x_{\text{ref}}(t) = x_1^*(t)$). In line with our discussion in Sec. III, in simulations we choose the cutoff film thickness h^* based on the thickness below which the Eckart streaming ceases to dominate the Schlichting and Rayleigh streaming, $h^* \approx (\lambda_{\text{oil}}/4)/\ell = 17 \mu\text{m}/\ell$.

We commence our analysis by considering the experimental case where an oil drop of a volume of 8 mm^3 is under the excitation of the 20 MHz SAW that supports a normal surface displacement amplitude of $A = 1.3$ nm before attenuation, shown in Fig. 4. Table I gives the corresponding dimensional and dimensionless parameters (see also Eqs. (9) and (10)). Figure 6(a) shows the evolution of the thickness profile obtained by solving Eq. (21) for the parameter values in Table I, subject to the initial condition given by Eq. (26), and boundary conditions fixing the film thickness to h_p and requiring vanishing derivatives at the domain boundaries. We observe that the simulated drop settles to a steady shape, which translates uniformly. The steady shape of the bulk droplet has a pronounced ‘‘foot’’ at its rear; though we do not yet fully understand the details of why this forms, it is consistent with the overall drop asymmetry that develops, see Fig. 2. We discuss these features of the results further below.

Figure 6(b) shows a single thickness profile at $t = 2$ s (blue curve), which is compared with the experimental data (black symbols). We note that capturing the spreading experimental drop geometry (and velocity) requires image analysis of the captured image data; the analysis adds uncertainty to the measured data estimated to be $\pm 50 \mu\text{m}$. Moreover, repeating experiments show some sensitivity to the initial condition, i.e., the thickness of the oil drop placed upon the SAW device at the time SAW is initiated, albeit in all cases the oil reaches a constant speed at long times.

B. Parametric dependence

In this section, we separate the discussion into two parts: first, we consider early-time behavior, and then long-time evolution. Figure 7 shows the computational results for the maximum drop height h_{max} for different values of A . We show the results for two different initial conditions, with the purpose of illustrating the relevance of the initial drop shape. Focusing first on the initial condition used for Fig. 6 (solid curves in Fig. 7) with initial drop height of $h_d \approx 0.5$ obtained from the experiments (see also Eq. (25)), we note different behavior for small and large values of A , as could be anticipated from the experimental results of Fig. 4(b). For the larger A -values, h_{max} initially increases

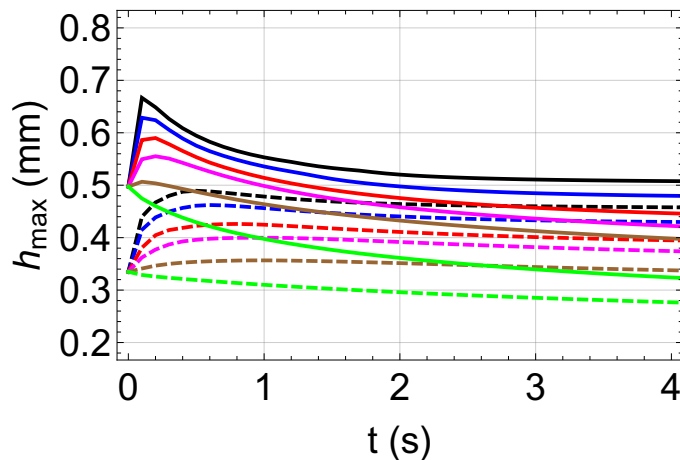


FIG. 7. Maximum fluid thickness, h_{\max} , as a function of time for two initial conditions of the drop: $r_d = 3.2$ (solid lines) and $r_d = 3.9$ (dashed lines) (in units of ℓ). The cross-sectional fluid area, A_d , is the same, but the latter has a lower initial maximum thickness than the former (see Eq. (25)). The values of A are: 2.00 nm (black), 1.69 nm (blue), 1.30 nm (red), 1.04 nm (magenta), 0.65 nm (brown), 0.20 nm (green).

rapidly but then decreases. For the two smallest A -values, this initial rapid increase is not observed. In all cases, for longer times, h_{\max} slowly decreases towards a constant (A -dependent) value, although it does not completely saturate for the times shown. One interpretation of these results is that for large A , the acoustic forcing dominates capillary stresses and gravity, leading to an increase of the drop height, while for smaller A , the acoustic forcing is not strong enough to lead to initial drop height increase. For the other initial condition (smaller initial drop height, shown by dashed lines in Fig. 7), the details are different, but we again observe an initial increase of h_{\max} for sufficiently large values of A , followed by (in this case) a slight decrease towards constant A -dependent values at large times.

Next, we shift our attention to long-time behavior, focusing first on the dependence of drop profiles on SAW amplitude. Figure 8 shows the long-time drop profiles together with the dimensionless pressure specified by Eq. (22) for four values of A . While the maximum drop height increases with A , as expected, we note that the thickness of the ‘foot’ directly behind the front increases with A as well (varying between approximately 50 and 100 μm for the considered values of A). In addition, we note a very thin trailing film, just slightly thicker than the precursor left behind the translating drop. While both the ‘foot’ and the thin trailing film still need to be fully analyzed and understood, we suspect that these features of the results are related to the pressure (plotted by the red lines with values shown on the right-hand axis in Fig. 8); note that the ‘foot’ forms in the region where the dimensionless pressure is $O(1)$, shown by the dashed lines. On a different note, we point out the strong decrease of the pressure due to the SAW attenuation, as the film height increases from the precursor scale, as well as the pressure dip at the front contact line, caused by the rapidly changing curvature there.

Focusing next on the spreading speed, Fig. 9 illustrates that for long times both experiments and simulations show approximately constant spreading speed (drop front position x_f increasing linearly in time), which seems to be a characteristic feature of the considered acoustic driving (note that we shift the experimental results in the figure to illustrate better the long time behavior; initial transients may account for differences at early times due to the particulars of the initial conditions). These results suggest that the spreading drop essentially translates without much shape change at late times. Figure 10(a) confirms this expectation: this figure shows that the width of the spreading drop, $w = x_2^* - x_1^*$, reaches a plateau and remains constant in the case of larger acoustic amplitudes A ; on sufficiently long time scales (not shown in the figure), the w -values obtained for smaller A -values reach a plateau as well.

To summarize our numerical results, Fig. 10(b) plots the numerically-predicted long-time values (reached for $t \gtrsim 6$ s) of the front velocity, v_f , the maximum drop height, h_{\max} , and the drop width, $w = x_2^* - x_1^*$, as a function of A . We note that, while v_f strongly increases with A , the dependence of h_{\max} and w on A is much weaker. These results suggest that a good qualitative description of the problem might be obtained by considering a traveling wave type of solution. Such an approach is discussed in the following section.

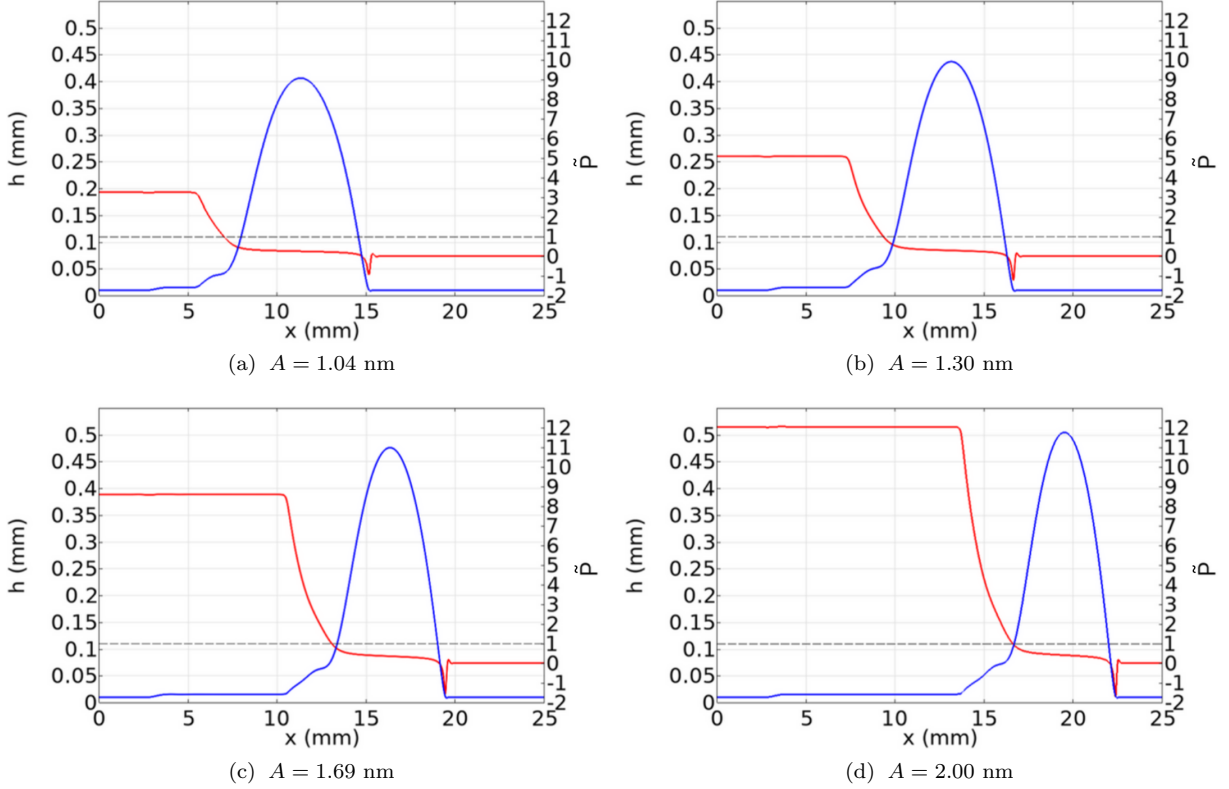


FIG. 8. Simulated drop profiles (blue curves, left axis) and dimensionless pressure \tilde{P} (red curves, right axis) at $t = 6$ s for four different values of A . The horizontal dashed line is at $\tilde{P} = 1$.

C. Traveling wave solution

In view of the results presented so far, we now seek a traveling wave solution of Eq. (21). Within this framework, we assume that the whole drop translates by constant speed U , so that

$$x_r(t) = Ut, \quad x_f(t) = w + Ut, \quad (28)$$

where (constant) w is the width of the moving drop. Here, we will consider that the rear (front) contact lines of the traveling drop are given by x_1^* (x_2^*) (see Fig. 5), since the SAW force that drives it is felt only where $h > h^*$. Then, we define $\xi = x - x_1^*(t) = x - Ut$ and assume that $h(x, t) = h(\xi)$, so that Eq. (21) becomes (see also [57, 58, 59] for similar studies without SAW forces)

$$U \frac{dh}{d\xi} + \frac{d}{d\xi} \left[h^3 \frac{d}{d\xi} \left(-\frac{d^2h}{d\xi^2} + \text{Bo} h + S\phi_s(\xi, h) \right) \right] = 0, \quad (29)$$

where

$$\phi_s(\xi, h) = e^{-2k_i[\xi + \alpha_1(h - h^*)]}. \quad (30)$$

This equation can be integrated once to yield

$$Uh + h^3 \frac{d}{d\xi} \left[-\frac{d^2h}{d\xi^2} + \text{Bo} h + S\phi_s(\xi, h) \right] = J, \quad (31)$$

where J represents the flux. The traveling wave solution must be calculated for $0 \leq \xi \leq \xi_f$, along with the following boundary conditions at $\xi = 0$

$$h(0) = h^*, \quad h'(0) = h'''(0) = 0, \quad (32)$$

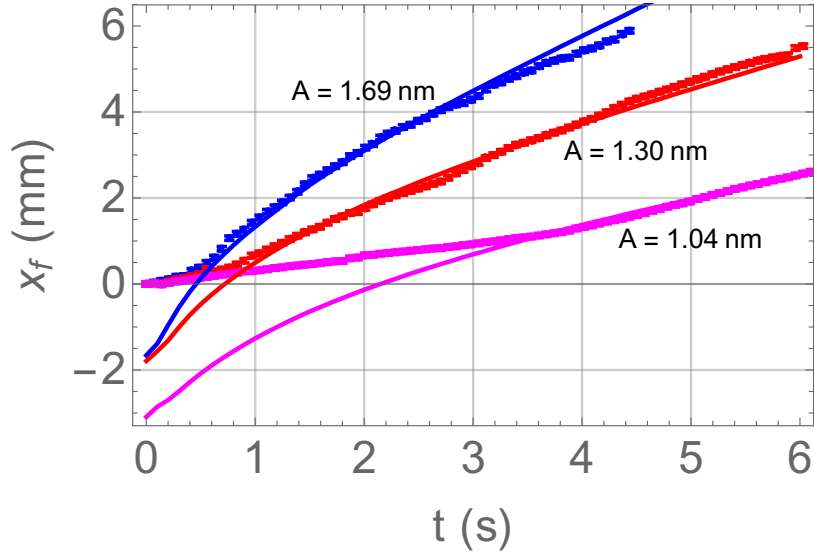


FIG. 9. Comparison between numerical (solid lines) and experimental (symbols) results for $A = 1.69$ nm (blue), 1.30 nm (red) and 1.04 nm (magenta). We have added arbitrary x -shifts to the simulation results to facilitate the comparison of the slope of x_f versus t between experiments and simulations for long times.

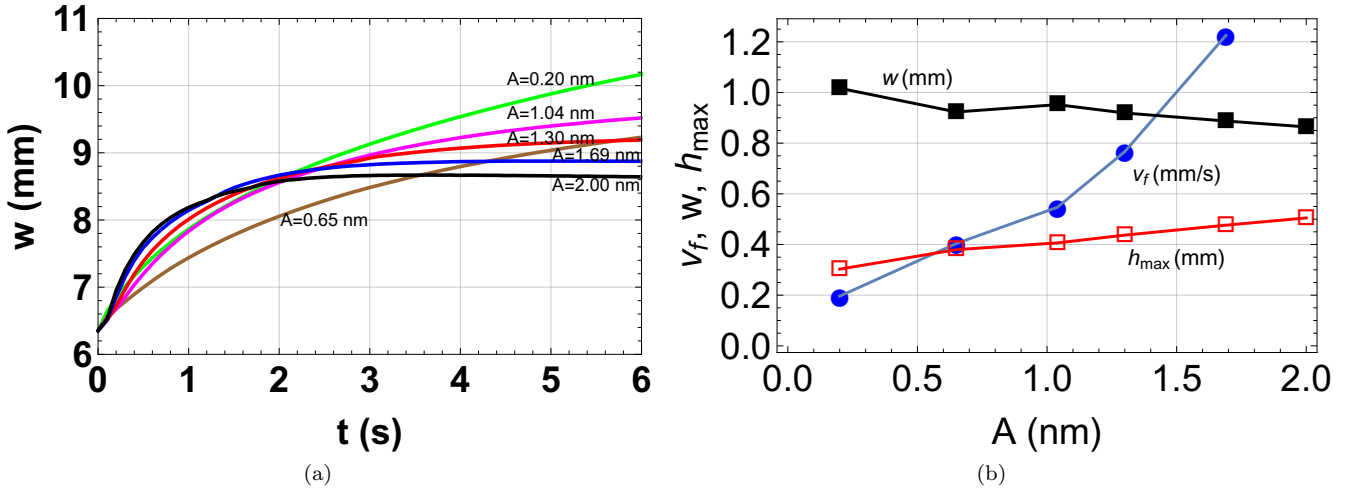


FIG. 10. (a) Numerically calculated drop width, w , as a function of time for several values of A : $A = 0.20$ nm (green), $A = 0.65$ nm (brown), $A = 1.04$ nm (magenta), $A = 1.30$ nm (red), $A = 1.69$ nm (blue), and $A = 2.00$ nm (black). Note that the two smallest values of A have not reached an asymptotic value of w for $t = 6$ s, but will do for later times. (b) Long time values of the front speed, v_f (in mm/s, blue filled circles), maximum thickness, h_{\max} (mm, red hollow squares), and drop width, w (mm, black filled squares), as functions of A . The points correspond to the raw data, and the solid lines connecting them guide the eye.

where the prime denotes $d/d\xi$. The values of $h''(0)$, U and ξ_f are determined by

$$h(\xi_f) = h^*, \quad J(0) = J(\xi_f), \quad A_d = \int_0^{\xi_f} h(\xi) d\xi. \quad (33)$$

Note that J corresponds to the flux within a thin film of thickness h^* that enters the drop at ξ_f and comes out of it at $\xi = 0$ (with respect to the reference frame fixed at the drop). Also, note that ξ_f is exactly the width of the traveling drop, w .

We developed an iterative scheme to perform the numerical integration of Eq. (31), under the conditions given by Eq. (33). We start by guessing values of $h''(0)$, U and ξ_f to perform the integration of Eq. (31) and modify them accordingly until these conditions are satisfied within a small relative error (typically, 10^{-7}). After obtaining

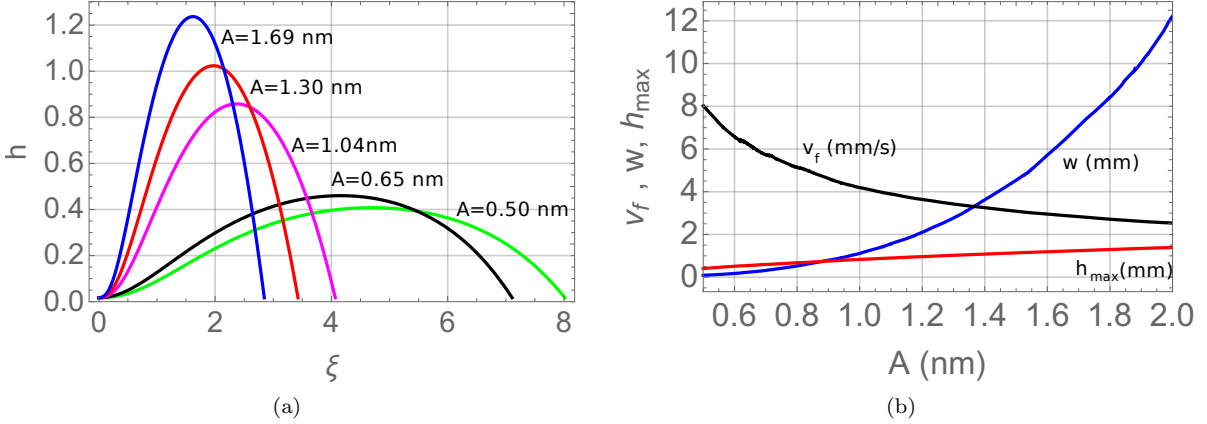


FIG. 11. (a) Thickness profile of the traveling wave solution for: $A = 0.50$ nm (green), 0.65 nm (black), 1.04 nm (magenta), 1.30 nm (red), 1.69 nm (blue). (b) Front speed, v_f (mm/s, black line), drop width, w (mm, blue line), and maximum height, h_{\max} (mm, red line), of the traveling drop as a function of A .

convergence for a given A , we use these converged values of $h''(0)$, U and ξ_f as new guess values for $A + \Delta A$ (continuation). ΔA has to be very small to reach convergence (typically, $\Delta A = 10^{-5}$ nm). Figure 11(a) shows the drop profiles for the values of A considered so far. Clearly, drops became taller and narrower as A increases. To compare the results with the experimental ones, we note that for $A = 1.3$ nm, the dimensional drop speed is $v_f = (\ell/t_c)U = 2.75$ mm/s, which is of the order of the experimental value. As expected, the value of J is small compared to unity, $J = 3.26 \times 10^{-4}$. Figure 11(b) shows the dependence of drop speed, v_f , its width, w , and the maximum thickness, h_{\max} , on A . Note that the model predicts that the speed depends approximately quadratically on the amplitude, A , as expected since the drop thickness increases linearly with A . We note that the trends shown in this figure for the traveling wave are similar to those in Fig. 10(b) obtained using the full numerical solution.

This approximate formulation shows that the simple traveling-wave solution can capture, at least qualitatively, features of the experimental drops. Clearly, however, this description cannot account for the rear flat film left behind the drop and the fact that the actual rear contact line remains practically at rest.

We note that we can use these results also to obtain an approximate value of U by applying a simple formula to estimate the front speed, v_f . By setting $J \approx 0$ and neglecting both capillary and gravity effects in Eq. (29), we have

$$U \approx -Sh^2 \frac{d\phi_s}{d\xi} = 2k_i Sh^2 e^{-2k_i[\xi + \alpha_1(h-h^*)]}. \quad (34)$$

By setting $h = h_d/\ell$ and $\xi = 2r_d/\ell$, this expression yields $v_f = U\ell/t_c = 0.4$ mm/s for $A = 1.3$ nm, which is the right order of magnitude.

V. CONCLUSIONS

In this work, we consider experimentally, theoretically, and computationally the problem of a spreading silicone oil drop driven by a surface acoustic wave (SAW) propagating in the supporting substrate. Our particular focus is on drops of millimetric thickness, for which the main driving mechanism is the Eckart streaming. Therefore, we are considering a different regime from that relevant for much thinner drops, for which Schlichting and Rayleigh streaming effects are dominant. To the best of our knowledge, modeling the dynamics of millimetric drops under the action of SAW and capillary stresses has not been considered so far in the literature.

While developing our theoretical description of drop spreading, it became apparent that a crucial effect, which requires careful modeling, involves the attenuation of the SAW under the evolving drop. The model we derived, assuming the thin film limit and implementing the long-wave approximation, shows that the drop is essentially pushed by the SAW forcing from behind, in contrast to situations where flow is driven by a body force such as gravity (for example, spreading on an inclined plane). A consequence of the driving mechanism is that the dynamics itself is substantially different from the familiar case of drops driven by gravity, where the volume force is a constant and not rapidly decreasing along the drop, as it occurs with the SAW force. In particular, we find that the drops tend to keep almost the same shape with time and spreading progress, and also that they reach essentially constant spreading

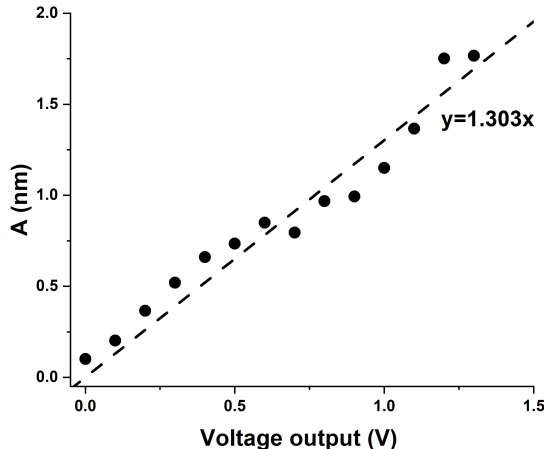


FIG. 12. A calibration plot of corresponding SAW displacement when different voltages are applied to the actuator.

speed at long times. This contrasts with the gravity-driven case, where the spreading speed decreases due to drop thinning. The main features of our theoretical and computational results are in reasonable qualitative and sometimes even quantitative agreement with the experiments, supporting further the basic premises leading to the developed acousto-fluidic model.

While not all details of the experimental results are fully understood, in general, we find very reasonable agreement between the experiments and theoretical results, in particular regarding drop shapes, spreading speeds, and the dependence of the results on the SAW displacement amplitude at the solid surface (intensity). Both theoretical and experimental results show asymmetric drop shapes with a thin film left behind, and both appear to be reaching a constant spreading speed asymptotically in time. The latter finding motivated us to formulate a simplified traveling wave model. The resulting analytical solution predicts a linear increase in the drop thickness and a quadratic increase of the spreading speed with the acoustic intensity (SAW normal displacement amplitude at the solid surface), A . Such predicted trends are consistent with the predictions of the full theoretical model and the experiments.

While many features of the experimental results have been rationalized using our theoretical models and simulations, much remains to be done. Further investigation is required to shed light on the features of dynamic drop profiles under SAW excitation. The transition from three-dimensional (3D) to quasi-two-dimensional (2D) dynamics is also intriguing: under strong SAW excitation, a drop spreads along the path of the SAW and may be described to leading order using the 2D model given here. However, at weak SAW excitation, where the drop also spreads radially due to the relaxation of capillary stress at the free drop surface, the drop dynamics is inherently of the 3D type. Hence, 3D aspects of drop dynamics, in particular in cases where the contributions to flow from capillary and SAW stresses are comparable, remain to be simulated and understood. Furthermore, the main physical mechanisms involved in the formation of the trailing film behind the spreading drops should be understood in more detail.

Appendix A: Calibration of applied voltage versus SAW displacement

We use the normal displacement amplitude (particle displacement of the SAW) at the solid surface, A , to represent the SAW strength (intensity). In the experiments, we control this amplitude by changing the applied voltage of the signal generator. Therefore, we conducted an experiment to obtain a calibration curve between the applied voltage and amplitude, as shown in Fig 12. We measure A over a surface of $1 \times 1 \text{ mm}^2$ about 2 mm away from the SAW actuator using laser doppler vibrometer. We find an approximately linear dependence of A on voltage, consistently with the literature [60].

Appendix B: Computational implementation

Equation (21) is written in a form convenient for the use of COMSOLTM Multiphysics PDE Coefficients Form. This package solves, by finite elements, a vectorial equation for the unknown vector $\vec{u} = (u_1, u_2, \dots, u_N)^T$. The equation

is of the form

$$\mathbf{e} \frac{\partial^2 \vec{u}}{\partial t^2} + \mathbf{d} \frac{\partial \vec{u}}{\partial t} + \nabla \cdot (-\mathbf{c} \nabla \vec{u} - \alpha \vec{u} + \gamma) + \beta \nabla \vec{u} + \mathbf{a} \vec{u} = \vec{f}, \quad (\text{B1})$$

where the coefficients of the N scalar equations are in the matrices \mathbf{e} , \mathbf{d} , γ , \mathbf{a} (of dimensions $N \times N$), α , β (of dimensions $N \times N \times n$), \mathbf{c} (of dimensions $N \times N \times n \times n$) and the vector \vec{f} (of dimension N), where n is the spatial dimension of the problem ($n = 1, 2, 3$). In index notation, this equation reads as

$$e_{ij} \frac{\partial^2 u_j}{\partial t^2} + d_{ij} \frac{\partial u_j}{\partial t} + \frac{\partial}{\partial x_l} \left(-c_{ijkl} \frac{\partial u_j}{\partial x_k} - \alpha_{ijl} u_j + \gamma_{il} \right) + \beta_{ijl} \frac{\partial u_j}{\partial x_l} + a_{ij} u_j = f_i, \quad (\text{B2})$$

where $i, j = 1, \dots, N$ and $k, l = 1, \dots, n$.

The considered system, given by Eq. (21), contains two components $u = (\tilde{h}, \tilde{P})$ ($N = 2$) and we use two equations, namely, Eqs. (21) and (22) for ($n = 1$), corresponding to the solution depending on a single spatial variable, x .

In the following, we list the non-vanishing coefficients (we omit the indexes k and l for brevity and consider $x_1 \equiv x$ since $k = l = 1$):

- Row 1 ($i = 1$) for Eq. (21)

$$d_{11} = 1, \quad c_{12} = \tilde{h}^3. \quad (\text{B3})$$

- Row 2 ($i = 2$) for Eq. (22)

$$c_{21} = -1, \quad a_{21} = -\text{Bo}, \quad a_{22} = 1, \quad f_2 = \mathcal{S} \tilde{\phi}_s \quad (\text{B4})$$

At the domain ends, we apply Dirichlet boundary conditions $\tilde{h} = \tilde{h}_p$, where \tilde{h}_p is the precursor film thickness, and $\partial h / \partial x = 0$. In order to achieve convergent numerical simulations, we discretize the domain using $\Delta x = h_p$.

Declaration of Interests

The author report no conflict of interest.

-
- [1] F. Holly and M. Lemp, Wettability and wetting of corneal epithelium, *Experimental Eye Research* **11**, 239 (1971)
 - [2] E. Veldhuizen and H. Haagsman, Role of pulmonary surfactant components in surface film formation and dynamics, *Biochimica et Biophysica Acta (BBA) - Biomembranes* **1467**, 255 (2000)
 - [3] E. Dussan V. and R. Chow, On the ability of drops or bubbles to stick to non-horizontal surfaces of solids, *J. Fluid Mech.* **137**, 1 (1983)
 - [4] E. B. Dussan V. and S. H. Davis, On the motion of a fluid-fluid interface along a solid surface, *J. Fluid Mech.* **65**, 71 (1974)
 - [5] J. Atencia and D. Beebe, Controlled microfluidic interfaces, *Nature* **437**, 648 (2005)
 - [6] H. Stone, A. Stroock, and A. Ajdari, Engineering flows in small devices, *Ann. Rev. Fluid Mech.* **36**, 381 (2004)
 - [7] G. Whitesides, The origins and the future of microfluidics, *Nature* **442**, 368 (2006)
 - [8] C. Amon, J. Murthy, S. Yao, S. Narumanchi, C. Wu, and C. Hsieh, MEMS-enabled thermal management of high-heat-flux devices EDIFICE: embedded droplet impingement for integrated cooling of electronics, *Exp. Thermal Fluid Sci.* **25**, 231 (2001)
 - [9] A. Bar-Cohen, M. Arik, and M. Ohadi, Direct liquid cooling of high flux micro and nano electronic components, *Proc. IEEE* **94**, 1549 (2006)
 - [10] L. Fletcher, V. Sernas, and L. Galwin, Evaporation from thin water films on horizontal tubes, *Ind. Eng. Chem. Process Design Development* **13**, 265 (1974)
 - [11] J. Fendler, Self assembled nanostructured materials, *Chem. Materials* **8**, 1616 (1996)
 - [12] K. Nagayama, Two-dimensional self-assembly of colloids in thin liquid films, *Colloids Surf. A* (1996)
 - [13] J. Wang, Z. Zheng, H. Li, W. Huck, and H. Siringhaus, Dewetting of conducting polymer inkjet droplets on patterned surfaces, *Nature Materials* **3**, 171 (2004)
 - [14] A. Oron, S. H. Davis, and S. G. Bankoff, Long-scale evolution of thin liquid films, *Rev. Mod. Phys.* **69**, 931 (1997)
 - [15] R. Craster and O. Matar, Dynamics and stability of thin liquid films, *Rev. Mod. Phys.* **81**, 1131 (2009)
 - [16] M. Morozov and O. Manor, Vibration-driven mass transfer and dynamic wetting, *Current Opinion in Colloid & Interface Science* **36**, 37 (2018)
 - [17] P. Brunet, J. Eggers, and R. Deegan, Vibration-induced climbing of drops, *Phys. Rev. Lett.* **99**, 144501 (2007)
 - [18] P. Brunet, J. Eggers, and R. Deegan, Motion of a drop driven by substrate vibrations, *Eur. Phys. J. Special Topics* **166**, 11 (2009)

- [19] L. Yeo and J. Friend, Surface acoustic wave microfluidics, *Ann. Rev. Fluid Mech.* **46**, 379 (2014)
- [20] L. Rayleigh, On the circulation of air observed in Kundt's tubes, and on some allied acoustical problems, *Phil. Trans. Royal Soc. London* **175**, 1 (1884)
- [21] H. Schlichting, Calculation of even periodic barrier currents, *Phys. Z.* **33**, 327 (1932)
- [22] M. Longuet-Higgins, Mass Transport in Water Waves, *Philosophical Transactions of the Royal Society of London A* **245**, 535 (1953)
- [23] O. Manor, L. Yeo, and J. Friend, The appearance of boundary layers and drift flows due to high-frequency surface waves, *J. Fluid Mech.* **707**, 482–495 (2012)
- [24] J. Lighthill, Acoustic streaming, *J. Sound Vib.* **61**, 391 (1978)
- [25] C. Eckart, Vortices and streams caused by sound waves, *Phys. Rev.* **73**, 68 (1948)
- [26] W. Nyborg, Acoustic streaming due to attenuated plane waves, *J. Acoust. Soc. Am.* **25**, 1 (1952)
- [27] A. Wixforth, Acoustically driven planar microfluidics, *Superlattices and Microstructures* **33**, 389 (2003)
- [28] A. Wixforth, C. Strobl, C. Gauer, A. Toegl, J. Scriba, and Z. von Gutfenberg, Acoustic manipulation of small droplets, *Anal. Bioanal. Chem.* **379**, 982 (2004)
- [29] P. Brunet, M. Baudoin, O. Matar, and F. Zoueshtiagh, Droplet displacements and oscillations induced by ultrasonic surface acoustic waves: A quantitative study, *Phys. Rev. E* **81**, 036315 (2010)
- [30] Z. Gutfenberg, A. Rathgeber, S. Keller, J. Rädler, A. Wixforth, M. Kostur, M. Schindler, and P. Talkner, Flow profiling of a surface-acoustic-wave nanopump, *Phys. Rev. E* **70**, 056311 (2004)
- [31] S. Shiokawa, Y. Matsui, and T. Ueda, Liquid streaming and droplet formation caused by leaky Rayleigh waves, *Proc. IEEE Ultras. Symp.* **1**, 643 (1989)
- [32] R. Arzt, E. Salzman, and K. Dransfeld, Elastic surface waves in quartz at 316 MHz, *Appl. Phys. Lett.* **10**, 165 (1967)
- [33] P. Brunet, M. Baudoin, O. B. Matar, and F. Zoueshtiagh, Droplet displacements and oscillations induced by ultrasonic surface acoustic waves: A quantitative study, *Phys. Rev. E* **81**, 036315 (2010)
- [34] J. Campbell, Propagation of surface waves at the boundary between a piezoelectric crystal and a fluid medium, *IEEE Trans. Sonics Ultrason.* **17**, 71 (1970)
- [35] B. Chu and R. E. Apfel, Acoustic radiation pressure produced by a beam of sound, *J. Acoust. Society. Am.* **72**, 1673 (1982)
- [36] J. T. Karlsen, P. Augustsson, and H. Bruus, Acoustic force density acting on inhomogeneous fluids in acoustic fields, *Phys. Rev. Lett.* **117**, 114504 (2016)
- [37] V. Rajendran, R. S. Aravind, and K. Subramani, On the stability of inhomogeneous fluids under acoustic fields, *J. Fluid Mech.* **964**, A23 (2023)
- [38] F. Borgnis, Acoustic radiation pressure of plane compressional waves, *Rev. Mod. Phys.* **25**, 653 (2010)
- [39] T. Hasegawa, T. Kido, T. Iizuka, and C. Matsuoka, A general theory of Rayleigh and Langevin radiation pressure, *J. Acoust. Soc. Jap.* **E 21**, 146 (2000)
- [40] L. King, On the acoustic radiation pressure on spheres, *Proc. R. Soc. Lond. A* **147**, 212 (1934)
- [41] S. Alzuaga, J. Manceau, and F. Bastien, Motion of droplets on solid surface using acoustic radiation pressure, *J. Sound Vib.* **282**, 151 (2005)
- [42] S. Biwersi, J. Manceau, and F. Bastien, Displacement of droplets and deformation of thin liquid layers using flexural vibrations of structures. Influence of acoustic radiation pressure, *J. Acoust. Soc. Am.* **107**, 661 (2000)
- [43] V. Rajendran, S. Jayakumar, M. Azharudeen, and K. Subramani, Theory of nonlinear acoustic forces acting on inhomogeneous fluids, *J. Fluid Mech.* **940**, A32 (2022)
- [44] A. Rezk, O. Manor, J. Friend, and L. Yeo, Unique fingering instabilities and soliton-like wave propagation in thin acoustowetting films, *Nat. Commun.* **3**, 1167 (2012)
- [45] A. Rezk, O. Manor, L. Yeo, and J. Friend, Double flow reversal in thin liquid films driven by MHz order surface vibration, *Proc. R. Soc. Lond. A* **470**, 20130765 (2014)
- [46] G. Altshuler and O. Manor, Spreading dynamics of a partially wetting water film atop a MHz substrate vibration, *Phys. Fluids* **27**, 102103 (2015)
- [47] G. Altshuler and O. Manor, Free films of a partially wetting liquid under the influence of a propagating mhz surface acoustic wave, *Phys. Fluids* **28**, 072102 (2016)
- [48] S. Mhatre, A. Zigelman, L. Abezgauz, and O. Manor, Influence of a Propagating Megahertz Surface Acoustic Wave on the Pattern Deposition of Solute Mass off an Evaporating Solution, *Langmuir* **32**, 9611 (2016)
- [49] J. Campbell and W. Jones, A method for estimating optimal crystal cuts and propagation directions for excitation of piezoelectric surface waves, *IEEE Trans. Sonics Ultrason.* **15**, 209 (1968)
- [50] D. Brown and A. Cox, Innovative uses of video analysis, *The Physics Teacher* **47**, 145 (2009)
- [51] S. Shiokawa, Y. Matsui, and T. Ueda, Study on saw streaming and its application to fluid devices, *Jap. J. Applied Physics* **29**, 137 (1990)
- [52] Roditi, Lithium niobate wafers - applications and specifications, <https://www.roditi.com/SingleCrystal/LiNbO3/LiNbO3-Wafers.html> (2023)
- [53] PrecisionFlow, Speed of sound in common materials for use with ultrasonic flow meters, <http://www.precisionflow.co.uk> (2023)
- [54] M. Hamilton and D. Blackstock, *Nonlinear Acoustics* (Academic Press, 1998)
- [55] L. Kondic, Instability in the gravity driven flow of thin liquid films, *SIAM Review* **45**, 95 (2003)
- [56] J. Diez and L. Kondic, Computing three-dimensional thin film flows including contact lines, *J. Comput. Phys.* **183**, 274 (2002)
- [57] B. R., M. Shearer, and A. Bertozzi, Thin film traveling waves and the navier slip condition, *SIAM J. Appl. Math.* , 722

(2003)

- [58] C. A. Perazzo and J. Gratton, Steady and traveling flows of a power-law liquid over an incline, [Journal of Non-Newtonian Fluid Mechanics](#) **118**, 57 (2004)
- [59] L. Giacomelli, M. Gnann, and F. Otto, Rigorous asymptotics of traveling-wave solutions to the thin-film equation and tanner's law, [Nonlinearity](#) (2016)
- [60] D. Ballantine Jr, R. White, S. Martin, A. Ricco, E. Zellers, G. Frye, and H. Wohltjen, *Acoustic wave sensors: theory, design and physico-chemical applications* (Elsevier, 1996)